

CHALMERS
UNIVERSITY OF TECHNOLOGY

Investigation of Control Parameters' Impact on Damping Property of Grid-Forming Converters

Downloaded from: https://research.chalmers.se, 2026-11-23 00:27 UTC

Citation for the original published paper (version of record):
Kamalinejad, K., Narula, A., Bongiorno, M. et al (2024). Investigation of Control Parameters' Impact on Damping Property of Grid-Forming Converters. 2024 IEEE Energy Conversion Congress and Exposition, ECCE 2024 - Proceedings. http://dx.doi.org/10.1109/ECCE55643.2024.10860863

N.B. When citing this work, cite the original published paper.

© 2024 IEEE. Personal use of this material is permitted. Permission from IEEE must be obtained for all other uses, in any current or future media, including reprinting/republishing this material for advertising or promotional purposes, or reuse of any copyrighted component of this work in other works.

(article starts on next page)

Investigation of Control Parameters' Impact on Damping Property of Grid-Forming Converters

Kavian Kamalinejad
Dept. of Electrical Engineering
Chalmers University of Technology
Göteborg, Sweden
kavian.kamalinejad@chalmers.se

Anant Narula
Dept. of Electrical Engineering
Chalmers University of Technology
Göteborg, Sweden
anant.narula@chalmers.se

Massimo Bongiorno
Dept. of Electrical Engineering
Chalmers University of Technology
Göteborg, Sweden
massimo.bongiorno@chalmers.se

Mebtu Beza
Dept. of Electrical Engineering
Chalmers University of Technology
Göteborg, Sweden
mebtu.beza@chalmers.se

Jan R. Svensson
Hitachi Energy Research
Hitachi Energy
Västerås, Sweden
jan.r.svensson@hitachienergy.com

***Abstract*—In this paper, the damping properties of two different grid-forming (GFM) control strategies, namely direct control of converter voltage (DCCV) and virtual-admittance based control (VABC) are investigated. The investigation is based on network frequency perturbation (NFP) plot, derived from linearized model of the system. The analysis indicates the distinct impact of GFM control parameters on damping at different frequency regions. Finally, the analytical findings are validated through detailed time-domain simulations in MATLAB/Simulink.**

***Keywords*—** Damping property, grid forming control, network frequency perturbation (NFP) plot.

I. Introduction

Aligned with efforts to decrease greenhouse gas emissions, the power system is experiencing a shift away from fossil fuel-based generation toward renewable energy sources (RES), often connected to the grid via voltage-source converters (VSCs) [1], [2]. As increased share of grid-connected power electronics might challenge the grid stability, grid-forming (GFM) converter control, emulating synchronous generators behavior, is proposed to deal with potential stability challenges [3]. A converter system with GFM capability should be able to create or form the system voltage, contribute to fault level (short-circuit power), contribute to the total system inertia, etc. Moreover, similar to synchronous machines, which should desirably have a positive damping and synchronizing power (the component of power change in phase with speed deviation and rotor angle perturbation, respectively) [4], it is desirable for GFM converters to have a positive contribution to the damping and synchronizing power to enhance the stability of future power system.

To analyze the damping provided by a GFM converter, non-linear and linear analysis methods can be utilized [5]. Electro-magnetic transient (EMT) based analysis and root mean squared (RMS) based analysis are two non-linear tools. The core principle of EMT-based time-domain analysis tools is that they take into account the instantaneous values of voltage and current, unlike RMS-based tools, which only consider values at the fundamental frequency. When a balance between computational effort and simulation accuracy is crucial, RMS-based tools are more appropriate compared with EMT-based analysis for analyzing the dynamic stability of large-scale power systems around a fundamental frequency [6].

On the other hand, while non-linear analysis might require more computational efforts, linear analyses, including time domain and frequency domain methods, are widely used to give rapid results and analyze the dynamic behaviour of the system [7]. Therefore, these methods can be used to understand the impact of system and control parameters analytically. State-space method, categorized as a time domain analysis, provides information about the damping ratio and natural frequency of the system, which are obtained from the eigenvalues. However, to obtain the eigenvalues, all the parameters of the system should be available [8]. In contrast to the state-space method, using network frequency perturbation (NFP) plot or passivity-based methods as linear analyses in the frequency domain offer valuable insights to system operators, particularly in cases where the plant is treated as a black box, concealing details such as the control system and exact component [9], [10]. NFP plots can be used to represent the behavior of a grid-connected generation source during grid frequency or voltage disturbances. For these reasons, NFP plots have been recommended for compliance testing of GFM plants in the recent grid codes [5], [11].

The aim of this paper is to analyze and show the damping properties of the GFM converters. To investigate this, the effects of related control parameters of two different GFM control strategies, named direct control of converter voltage (DCCV) and virtual-admittance based control (VABC), are examined. The examination is based on analyzing NFP plots obtained from the linearized model of the under-study system, so as to understand the impact of the control parameters in different frequency regions, with focus on the sub-synchronous

frequency range. Then, to validate the damping analysis based on NFP plot, time-domain simulation results are presented.

The rest of the paper is organized as follows: Section II describes the system under study and controllers. The linearized equations are derived in Section III to obtain the NFP plots. In Section IV, damping properties of the GFM converter are discussed and verified based on NFP plots and time-domain simulation, respectively. Finally, conclusions are drawn in Section V.

II. System and Controllers Description

In this section, two GFM control strategies named DCCV and VABC are introduced and their differences are briefly highlighted. Moreover, the structure of the system under-study is presented.

As can be seen from Fig. 1(a), The system consists of a VSC connected to a series-compensated AC grid through an inductive filter and a step-up AC transformer. It is worth mentioning that the series compensator's capacitance is considered to have a tunable resonance frequency in the sub-synchronous region, which can be triggered to display the impact of control parameters in that region.

The control structure of DCCV and VABC is illustrated in Fig. 1(b) and Fig. 1(c), respectively. In DCCV, the references for the amplitude and the angle of the converter voltage are directly generated by the AC-voltage controller and the active-power controller, respectively. On the other hand, in VABC, the VSC appears like a virtual machine with a virtual back electromotive force (EMF) and a virtual impedance, including the physical converter filter and a tunable virtual part. Generally, while DCCV is less complex to implement, VABC has advantages over DCCV in terms of less dependency on grid strength as it increases the electrical distance between point-of-common-coupling (PCC) and the voltage that is controlled. Moreover, virtual inductance and resistance are the extra control parameters, providing more degree of freedom in controlling the system [12].

The synchronization angle θ, which corresponds to θ_c in DCCV and θ_{EMF} in VABC, is obtained from the active-power controller as:

$$\theta = \frac{1}{s}[\overbrace{(K_{p,pc} + \frac{K_{i,pc}}{s})}^{G_{pc}}(P_g^\star - P_g) - R_a P_g + \omega_N] \quad (1)$$

where ω_N is rated angular frequency (in rad/s) of the AC grid. Moreover, P_g and $P_g^\star$ are the injected active power and its reference, respectively. $K_{\text{p,pc}}$ and $K_{\text{i,pc}}$ denote the proportional and integral gains of the PI regulator, while R_{a} denotes a transient damping term which is included to improve the dynamic performance of the controller [13]. The parameters of the controller are selected in order to obtain a first order closed loop response from $P_g^\star$ to P_g.

The AC-voltage controller is based on an integrator with the gain of $K_{\text{i,vc}}$, which is used to regulate the magnitude of

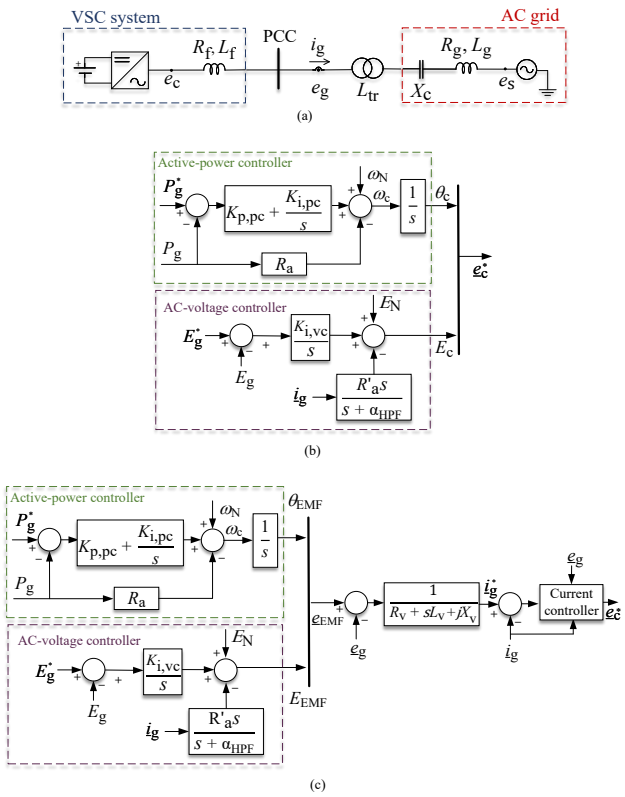


Figure 1: (a) Structure of the system under study. (b) Control structure of DCCV. (c) Control structure of VABC.

the voltage at the PCC (E_{g}) to its reference value ($E_g^\star$). In the block diagram, E_{N} is the rated system voltage, and $R_a^{'}$ is a transient damping term implemented through a high-pass filter with the bandwidth of α_{HPF} [12]. The AC-voltage controller relation can be written as:

$$\underline{e}^\star = E_{\text{N}} + \overbrace{\frac{K_{\text{i,vc}}}{s}}^{G_{\text{vc}}}(E_{\text{g}}^\star - E_{\text{g}}) - \overbrace{\frac{s}{s + \alpha_{\text{HPF}}}}^{G_{\text{HPF}}} R_a^{'} \underline{i}_g \quad (2)$$

It is worth mentioning that $\underline{e}^\star$ corresponds to $\underline{e}_c^\star$ in DCCV and $\underline{e}_{EMF}^\star$ in VABC. Moreover, variables with the underline represent vectors in converter dq-frame defined by the angle output of active-power controller (using power-invariant transformation), and capital letters signify the amplitude of the vector in this section.

In VABC strategy, in addition to active-power controller and AC-voltage controller, the virtual impedance should be implemented in the control system as shown in Fig. 1(c). L_v and R_v are the virtual inductance and resistance, respectively. In addition, X_v is the term coming from abc to dq transformation and is equal to $\omega_N L_v$. The virtual admittance calculates the reference current $\underline{i}_{\text{g}}^\star$, which is the input of the current controller, as:

$$\underline{i}_g^\star = \frac{\underline{e}_{\text{EMF}} - \underline{e}_{\text{g}}}{R_{\text{v}} + sL_{\text{v}} + jX_{\text{v}}} \quad (3)$$

The implemented current controller has a classical structure and is based on a PI regulator with cross-coupling cancellation and voltage feed-forward that is low-pass filtered with the cut-off frequency of α_{ff}. The current controller calculates the converter-voltage reference as [14]:

$$\underline{e}_{\mathrm{c}}^{\star} = \overbrace{\frac{\alpha_{\mathrm{ff}}}{s+\alpha_{\mathrm{ff}}}}^{H_{\mathrm{ff}}} \underline{e}_{\mathrm{g}} + j\omega_{\mathrm{N}} L_{\mathrm{f}} \underline{i}_{\mathrm{g}} + \overbrace{(K_{\mathrm{p,cc}} + \frac{K_{\mathrm{i,cc}}}{s})}^{G_{\mathrm{cc}}} (\underline{i}_{\mathrm{g}}^{\star} - \underline{i}_{\mathrm{g}}). \quad (4)$$

where L_f is the physical filter inductance. Moreover, $K_{p,cc}$ and $K_{i,pc}$ denote the proportional and integral gains of the PI regulator for the current controller, respectively.

III. Concept of Network Frequency Perturbation and Derivation of Linearized Model

In this section, the concept of NFP plots is discussed. Then, the linearized model of the system is derived to obtain the NFP plots. Finally, the NFP plots of investigated GFM strategies obtained from the linearized model are verified with the simulation results.

A. Network frequency perturbation (NFP) plot concept

The NFP plot was first introduced in [16]. It visually represents the amplitude and phase of the active power response of the device being tested, which is the VSC in this case, with respect to the applied frequency perturbation. Therefore, it is a form of bode plot representing the amplitude and phase of the resulting active power oscillation ($\Delta P_s \angle \varphi_{\Delta P_s}$) responding to an applied frequency perturbation ($\Delta f_s \angle \varphi_{\Delta f_s}$) across a frequency base. Thus, NFP response (R_{NFP}) could be stated as [5]:

$$R_{\mathrm{NFP}} = \frac{\Delta P_{\mathrm{s}} \angle \varphi_{\Delta P_{\mathrm{s}}}}{\Delta f_{\mathrm{s}} \angle \varphi_{\Delta f_{\mathrm{s}}}} \quad (5)$$

The NFP plot can be obtained from either a time-domain simulation, followed by the Fourier analysis, or from the linear analysis of the system and obtaining a closed-loop transfer function from the input grid frequency variation to the output active-power variation of a device. The NFP plot is typically obtained from PCC by modulating the frequency of a source voltage (f_{s}) in a sinusoidal fashion around the nominal frequency (f_{N}), as shown in Fig. 2(a). As an alternative, it is also possible to obtain NFP plot for the entire system to analyze the total system damping, as illustrated in Fig. 2(b). Therefore, while the former one reveals the characteristics of the converter, the later one possesses information about the whole system.

B. Derivation of the linearized equations to obtain the NFP plot

In this paper, in order to obtain the frequency response and, thereby, the NFP plots, the linearized model of the system is derived, and then, the correctness of the linearized model is verified by the NFP plots obtained in time-domain simulation. In the notations, Δ denotes the perturbation quantities, the subscript "0" represents steady-state quantities, and variables

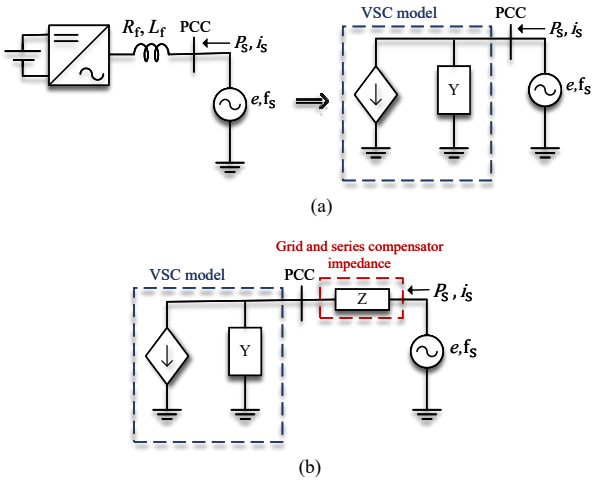


Figure 2: Network frequency perturbation implementation (a) from PCC, and (b) for the entire system.

with the underline represent vectors. Moreover, the voltage e represents e_{g} or e_{s} depending on the point where the frequency perturbation is applied.

The general active power relation is given as follows:

$$P_s = e_d^R i_{sd}^R + e_q^R i_{sq}^R \quad (6)$$

where superscript "R" denotes entities in a rotating dq-frame, which is defined by the angle θ_{N}, obtained by integrating the rated angular frequency, ω_{N}, and having a zero initial phase.

Linearizing (6) results in:

$$\Delta P_s = i_{sd0}^R \Delta e_d^R + e_{d0}^R \Delta i_{sd}^R + i_{sq0}^R \Delta e_q^R + e_{q0}^R \Delta i_{sq}^R \quad (7)$$

Furthermore, the voltage vector in the rotating dq-frame can be written as

$$\underline{e}^R = e_0 \; e^{j(\theta_S - \theta_N)} \quad (8)$$

The variation of the voltage vector during a frequency perturbation can be obtained by linearizing (8) as

$$\Delta \underline{e}^R = j e_0 \; e^{j(\theta_{s0} - \theta_{N0})} \Delta\theta_s; \; \Delta\theta_s = \frac{\Delta\omega_s}{s} \quad (9)$$

Moreover, the input admittance matrix obtained from linearizing the control strategies, depicted in Fig. 1, around the operating point can be shown as

$$\begin{bmatrix} \Delta i_{sd}^R \\ \Delta i_{sq}^R \end{bmatrix} = \begin{bmatrix} Y_{dd} & Y_{dq} \\ Y_{qd} & Y_{qq} \end{bmatrix} \begin{bmatrix} \Delta e_d^R \\ \Delta e_q^R \end{bmatrix} \quad (10)$$

It is worth noting that in case of obtaining the input admittance for the entire system, transformer, series compensator, and grid impedance should also be considered. Using (9) and (10), the dq-components of current variation can be obtained as follows:

$$\Delta i_{sd}^R = \frac{e_0}{s} Y_{dq} \Delta\omega_s, \;\; \Delta i_{sq}^R = \frac{e_0}{s} Y_{qq} \Delta\omega_s \tag{11}$$

Now, by utilizing (7), (9) and (11), the variation in active power can be obtained as

$$\Delta P_s = Y_{dq} \frac{e_0^2}{s} \Delta\omega_s + i_{sq0} \frac{e_0}{s} \Delta\omega_s \tag{12}$$

Finally, the transfer function from the applied frequency perturbation to the active power variation can be obtained as follows:

$$\frac{\Delta P_s}{\Delta\omega_s} = Y_{dq} \frac{e_0^2}{s} + i_{sq0} \frac{e_0}{s} \tag{13}$$

It can be seen that the transfer function from variation in frequency to active power change is dependent on only one component of the input admittance matrix (Y_{dq}) as well as the voltage and current steady-state values. The input admittance of the converter for DCCV and VABC strategies is derived in the following, which will be used to obtain the NFP plots in the rest of the paper.

The input admittance of the converter is derived in a rotating *dq*-frame, which is defined by the angle $\theta_{\rm N}$, obtained by integrating the rated angular frequency, $\omega_{\rm N}$, and having a zero initial phase. For this, the controller dynamics described in Section II should be transformed to this frame (referred here as rotating *dq*-frame). By using (1) the angle $\theta_{\rm L}$ is given as

$$\theta_{\rm L} = \theta - \theta_{\rm N} = \frac{1}{s}[G_{\rm pc}(P_{\rm g}^\star - P_{\rm g}) - R_{\rm a} P_{\rm g}] \tag{14}$$

where $\theta_{\rm L}$ represents the phase-angle difference between the emulated-voltage source and the ideal-voltage source, and can be interpreted as the converter's load angle. Thus, any space-vector $\underline{y}$ defined in Section II can be transformed to the rotating dq-frame using the following relation

$$\underline{z}^R = \underline{y} e^{j\theta_{\rm L}} \tag{15}$$

1) Input admittance of DCCV strategy

For DCCV, using (2), (14) and (15), the small-signal model of the converter voltage reference in the rotating *dq*-frame can be expressed as

$$\begin{aligned}
\begin{bmatrix} \Delta e_{\rm cd}^{R\star} \\ \Delta e_{\rm cq}^{R\star} \end{bmatrix} &= \overbrace{\begin{bmatrix} -(e_{\rm cq0}^R + G_{\rm HPF} R'_{\rm a} i_{\rm gq0}^R) & G_{\rm vc}\cos\theta_{\rm L0} \\ (e_{\rm cd0}^R + G_{\rm HPF} R'_{\rm a} i_{\rm gd0}^R) & G_{\rm vc}\sin\theta_{\rm L0} \end{bmatrix}}^{\mathbf{G}_{\rm T}} \begin{bmatrix} \Delta\theta_{\rm L} \\ \Delta E_{\rm g}^\star \end{bmatrix} \\
&+ \left(- \overbrace{\begin{bmatrix} \frac{G_{\rm vc}\cos\theta_{\rm L0} e_{\rm gd0}^R}{E_{\rm g0}} & \frac{G_{\rm vc}\cos\theta_{\rm L0} e_{\rm gq0}^R}{E_{\rm g0}} \\ \frac{G_{\rm vc}\sin\theta_{\rm L0} e_{\rm gd0}^R}{E_{\rm g0}} & \frac{G_{\rm vc}\sin\theta_{\rm L0} e_{\rm gq0}^R}{E_{\rm g0}} \end{bmatrix}}^{\mathbf{G}_{\rm PVv1}} \right) \begin{bmatrix} \Delta e_{\rm gd}^R \\ \Delta e_{\rm gq}^R \end{bmatrix} \\
&+ \overbrace{\begin{bmatrix} -G_{\rm HPF} R'_{\rm a} & 0 \\ 0 & -G_{\rm HPF} R'_{\rm a} \end{bmatrix}}^{\mathbf{G}_{\rm DH}} \begin{bmatrix} \Delta i_{\rm gd}^R \\ \Delta i_{\rm gq}^R \end{bmatrix}
\end{aligned} \tag{16}$$

with

$$\begin{aligned}
\begin{bmatrix} \Delta\theta_{\rm L} \\ \Delta E_{\rm g}^\star \end{bmatrix} &= \begin{bmatrix} \frac{G_{\rm pc}}{s} & 0 \\ 0 & 1 \end{bmatrix} \begin{bmatrix} \Delta P_{\rm g}^\star \\ \Delta E_{\rm g}^\star \end{bmatrix} \\
&+ \overbrace{\begin{bmatrix} -\frac{(G_{\rm pc}+R_{\rm a}) e_{\rm gd0}^R}{s} & -\frac{(G_{\rm pc}+R_{\rm a}) e_{\rm gq0}^R}{s} \\ 0 & 0 \end{bmatrix}}^{\mathbf{G}_{\rm PVc2}} \begin{bmatrix} \Delta i_{\rm gd}^R \\ \Delta i_{\rm gq}^R \end{bmatrix} \\
&+ \overbrace{\begin{bmatrix} -\frac{(G_{\rm pc}+R_{\rm a}) i_{\rm gd0}^R}{s} & -\frac{(G_{\rm pc}+R_{\rm a}) i_{\rm gq0}^R}{s} \\ 0 & 0 \end{bmatrix}}^{\mathbf{G}_{\rm PVv2}} \begin{bmatrix} \Delta e_{\rm gd}^R \\ \Delta e_{\rm gq}^R \end{bmatrix}
\end{aligned} \tag{17}$$

where the expressions $P_{\rm g} = e_{\rm gd}^R i_{\rm gd}^R + e_{\rm gq}^R i_{\rm gq}^R$, and $E_{\rm g} = \sqrt{(e_{\rm gd}^R)^2 + (e_{\rm gq}^R)^2}$ are used for the active power injected into the grid and PCC-voltage magnitude, respectively. Now, by neglecting the impact of delays and using (16), (17) and the linearized expression for the current dynamics in the rotating *dq*-frame, which is given by

$$\begin{bmatrix} \Delta e_{\rm cd}^R \\ \Delta e_{\rm cq}^R \end{bmatrix} = \begin{bmatrix} \Delta e_{\rm gd}^R \\ \Delta e_{\rm gq}^R \end{bmatrix} + \overbrace{\begin{bmatrix} R_{\rm f} + sL_{\rm f} & -\omega_{\rm N} L_{\rm f} \\ \omega_{\rm N} L_{\rm f} & R_{\rm f} + sL_{\rm f} \end{bmatrix}}^{\mathbf{Z}_{\rm f}} \begin{bmatrix} \Delta i_{\rm gd}^R \\ \Delta i_{\rm gq}^R \end{bmatrix} \tag{18}$$

the small-signal model of the converter system in the rotating *dq*-frame is derived as

$$\begin{bmatrix} \Delta i_{\rm gd}^R \\ \Delta i_{\rm gq}^R \end{bmatrix} = \mathbf{G}_{\rm conv} \begin{bmatrix} \Delta P_{\rm g}^\star \\ \Delta E_{\rm g}^\star \end{bmatrix} - \mathbf{Y}_{\rm conv} \begin{bmatrix} \Delta e_{\rm gd}^R \\ \Delta e_{\rm gq}^R \end{bmatrix} \tag{19}$$

where $\mathbf{Y}_{\rm conv}$ denotes the input-admittance of the converter system seen from the PCC and is given by

$$\begin{aligned}
\mathbf{Y}_{\rm conv} = &[\mathbf{G}_{\rm T}\mathbf{G}_{\rm PVc2} + \mathbf{G}_{\rm DH} - \mathbf{Z}_{\rm f}]^{-1} \\
&[\mathbf{G}_{\rm T}\mathbf{G}_{\rm PVv2} - \mathbf{G}_{\rm PVv1} - \mathbf{I}]
\end{aligned} \tag{20}$$

with $\mathbf{I}$ denoting the identity matrix of dimension 2×2.

2) Input admittance of VABC strategy

For VABC, the small-signal model of the converter voltage reference in the rotating *dq*-frame can be obtained using (3), (4) and (15) as

$$\begin{aligned}
\begin{bmatrix} \Delta e_{\rm cd}^{R\star} \\ \Delta e_{\rm cq}^{R\star} \end{bmatrix} &= \overbrace{\begin{bmatrix} H_{\rm ff} - \frac{G_{\rm cc} R'_{\rm v}}{R'^2_{\rm v} + X_{\rm v}^2} & -\frac{G_{\rm cc} X_{\rm v}}{R'^2_{\rm v} + X_{\rm v}^2} \\ \frac{G_{\rm cc} X_{\rm v}}{R'^2_{\rm v} + X_{\rm v}^2} & H_{\rm ff} - \frac{G_{\rm cc} R'_{\rm v}}{R'^2_{\rm v} + X_{\rm v}^2} \end{bmatrix}}^{\mathbf{G}_{\rm ee}} \begin{bmatrix} \Delta e_{\rm gd}^R \\ \Delta e_{\rm gq}^R \end{bmatrix} \\
&+ \overbrace{\begin{bmatrix} -G_{\rm cc} & -\omega_{\rm N} L_{\rm f} \\ \omega_{\rm N} L_{\rm f} & -G_{\rm cc} \end{bmatrix}}^{\mathbf{Y}_{\rm i}} \begin{bmatrix} \Delta i_{\rm gd}^R \\ \Delta i_{\rm gq}^R \end{bmatrix} + \overbrace{\begin{bmatrix} \frac{G_{\rm cc} R'_{\rm v}}{R'^2_{\rm v} + X_{\rm v}^2} & \frac{G_{\rm cc} X_{\rm v}}{R'^2_{\rm v} + X_{\rm v}^2} \\ -\frac{G_{\rm cc} X_{\rm v}}{R'^2_{\rm v} + X_{\rm v}^2} & \frac{G_{\rm cc} R'_{\rm v}}{R'^2_{\rm v} + X_{\rm v}^2} \end{bmatrix}}^{\mathbf{Z}_{\rm v}} \begin{bmatrix} \Delta e_{\rm EMFd}^R \\ \Delta e_{\rm EMFq}^R \end{bmatrix} \\
&+ \overbrace{\begin{bmatrix} A_{\rm e} & 0 \\ B_{\rm e} & 0 \end{bmatrix}}^{\mathbf{G}_{\rm Te}} \begin{bmatrix} \Delta\theta_{\rm L} \\ \Delta E_{\rm g}^\star \end{bmatrix}
\end{aligned} \tag{21}$$

where $R'_{\rm v} = R_{\rm v} + sL_{\rm v}$ and the terms $A_{\rm e}$, $B_{\rm e}$ are given as

$$A_{\mathrm{e}} = -e^{R}_{\mathrm{cq0}} + H_{\mathrm{ff}} e^{R}_{\mathrm{gq0}} + i^{R}_{\mathrm{gd0}} \omega_{\mathrm{N}} L_{\mathrm{f}} - G_{\mathrm{cc}} i^{R}_{\mathrm{gq0}} + \frac{G_{\mathrm{cc}} e^{R}_{\mathrm{EMFq0}} R'_{\mathrm{v}} - G_{\mathrm{cc}} e^{R}_{\mathrm{EMFd0}} X_{\mathrm{v}}}{R'^{2}_{\mathrm{v}} + X^{2}_{\mathrm{v}}} + \frac{-G_{\mathrm{cc}} e^{R}_{\mathrm{gq0}} R'_{\mathrm{v}} + G_{\mathrm{cc}} e^{R}_{\mathrm{gd0}} X_{\mathrm{v}}}{R'^{2}_{\mathrm{v}} + X^{2}_{\mathrm{v}}};$$

$$B_{\mathrm{e}} = e^{R}_{\mathrm{cd0}} - H_{\mathrm{ff}} e^{R}_{\mathrm{gd0}} + i^{R}_{\mathrm{gq0}} \omega_{\mathrm{N}} L_{\mathrm{f}} + G_{\mathrm{cc}} i^{R}_{\mathrm{gd0}} - \frac{G_{\mathrm{cc}} e^{R}_{\mathrm{EMFd0}} R'_{\mathrm{v}} + G_{\mathrm{cc}} e^{R}_{\mathrm{EMFq0}} X_{\mathrm{v}}}{R'^{2}_{\mathrm{v}} + X^{2}_{\mathrm{v}}} + \frac{G_{\mathrm{cc}} e^{R}_{\mathrm{gd0}} R'_{\mathrm{v}} + G_{\mathrm{cc}} e^{R}_{\mathrm{gq0}} X_{\mathrm{v}}}{R'^{2}_{\mathrm{v}} + X^{2}_{\mathrm{v}}} \tag{22}$$

Furthermore, in analogy to (16), the small-signal model of the virtual back-EMF in the rotating *dq*-frame can be expressed using (2), (14) and (15) as

$$\begin{bmatrix} \Delta e^{R}_{\mathrm{EMFd}} \\ \Delta e^{R}_{\mathrm{EMFq}} \end{bmatrix} = \overbrace{\begin{bmatrix} -(e^{R}_{\mathrm{EMFq0}} + G_{\mathrm{HPF}} R'_{\mathrm{a}} i^{R}_{\mathrm{gq0}}) & G_{\mathrm{vc}} \cos\theta_{\mathrm{L0}} \\ (e^{R}_{\mathrm{EMFd0}} + G_{\mathrm{HPF}} R'_{\mathrm{a}} i^{R}_{\mathrm{gd0}}) & G_{\mathrm{vc}} \sin\theta_{\mathrm{L0}} \end{bmatrix}}^{\mathbf{G}'_{\mathrm{T}}} \begin{bmatrix} \Delta\theta_{\mathrm{L}} \\ \Delta E^{\star}_{\mathrm{g}} \end{bmatrix} + \mathbf{G}_{\mathrm{PVv1}} \begin{bmatrix} \Delta e^{R}_{\mathrm{gd}} \\ \Delta e^{R}_{\mathrm{gq}} \end{bmatrix} + \mathbf{G}_{\mathrm{DH}} \begin{bmatrix} \Delta i^{R}_{\mathrm{gd}} \\ \Delta i^{R}_{\mathrm{gq}} \end{bmatrix} \tag{23}$$

Finally, by neglecting the impact of delays and using (17), (18), (21) and (23), the input admittance of the converter system as seen from the PCC can be obtain as

$$\mathbf{Y}_{\mathrm{conv}} = [\mathbf{Y}_{\mathrm{i}} + \mathbf{Z}_{\mathrm{v}}\mathbf{G}_{\mathrm{DH}} + \mathbf{Z}_{\mathrm{v}}\mathbf{G}'_{\mathrm{T}}\mathbf{G}_{\mathrm{PVc2}} + \mathbf{G}_{\mathrm{Te}}\mathbf{G}_{\mathrm{PVc2}} - \mathbf{Z}_{\mathrm{f}}]^{-1} [\mathbf{G}_{\mathrm{ee}} + \mathbf{Z}_{\mathrm{v}}\mathbf{G}_{\mathrm{PVv1}} + \mathbf{Z}_{\mathrm{v}}\mathbf{G}'_{\mathrm{T}}\mathbf{G}_{\mathrm{PVv2}} + \mathbf{G}_{\mathrm{Te}}\mathbf{G}_{\mathrm{PVv2}} - \mathbf{I}] \tag{24}$$

C. Linearized model verification

To validate the linearized model derived above, the NFP plots for both DCCV and VABC strategies are obtained from the linearized equations and compared with the plots obtained using a detailed time-domain simulation model. The NFP plots from simulation are obtained from perturbation of the input grid frequency in MATLAB/Simulink, as discussed in Subsection III-A. The circuit and control parameters' values are presented in Table I.

Table I: CIRCUIT AND CONTROL PARAMETERS OF STUDIED GFM-VSCs

Parameter	Symbol	Unit
Nominal apparent power	S_{N}	100 MVA (1 pu)
Nominal RMS voltage	E_{N}	20 kV (1 pu)
Nominal frequency	f_{N}	50 Hz
Grid impedance (1/SCR)	L_{g}	1 pu
Series compensator impedance	X_{c}	0.125 pu
Active-power controller bandwidth	α_{pc}	5 Hz
Transient damping HPF bandwidth	α_{hpf}	5 Hz
Voltage controller bandwidth	α_{vc}	1 Hz
Filter resistance and inductance	R_{f}, L_{f}	0.015 pu, 0.15 pu
Transformer inductance	L_{tr}	0.15 pu
Virtual inductance (VAB strategy)	L_{v}	0.5 pu
Virtual resistance (VAB strategy)	R_{v}	0.25 pu

It can be seen from Fig. 3 that the NFP plots from the linearized and simulation model are matched. Therefore, the linearized model can be used for further analyses.

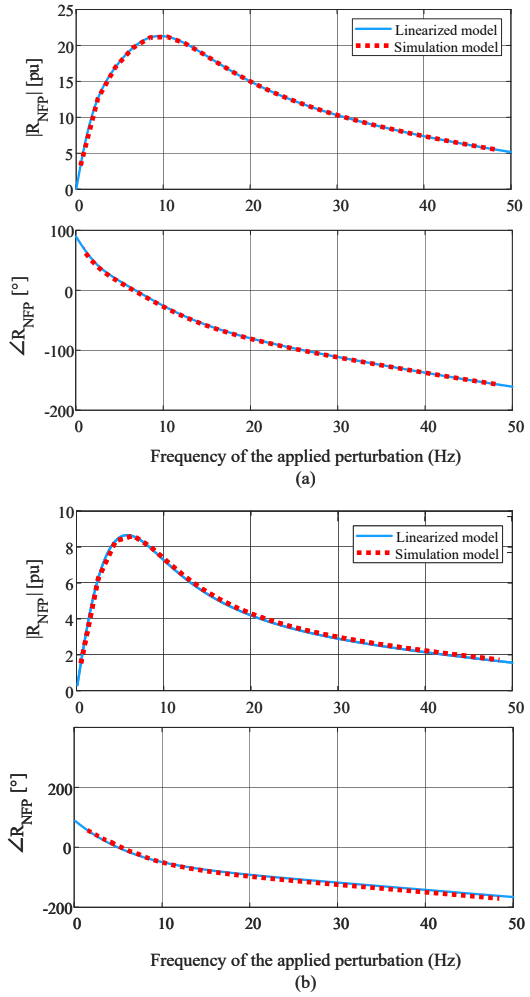


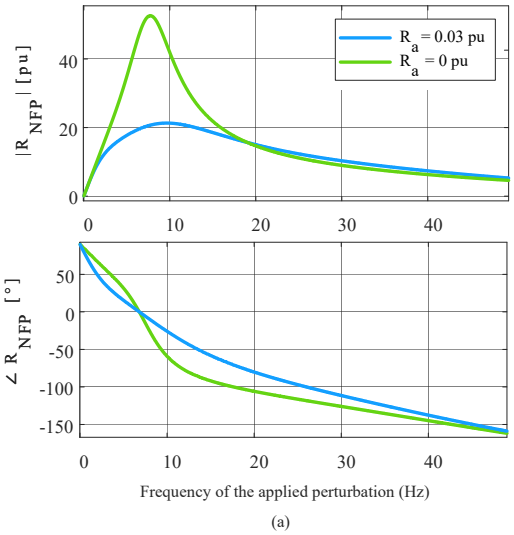
Figure 3: Comparison of NFP plots of the converter with DCCV and VABC strategies from linearized model and simulation. (a) DCCV strategy (b) VABC strategy

IV. Damping Property Evaluation of the GFM Control Strategies

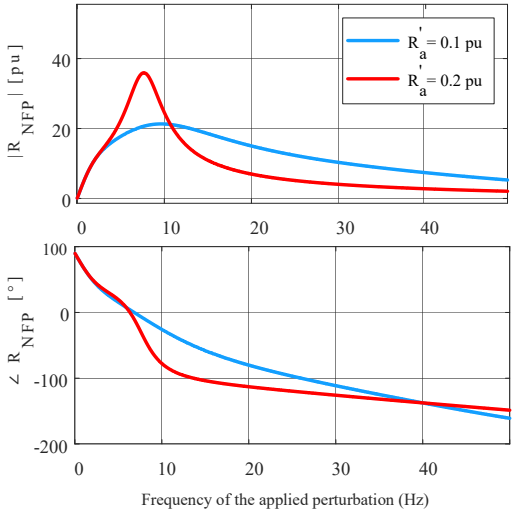
In this section, the NFP plots for the DCCV and VABC GFM converters and the entire system are obtained based on different values of converter's control parameters to analyze the damping properties. Then, the damping analysis is validated by time-domain simulation results.

A. Analyzing damping property using NFP plot

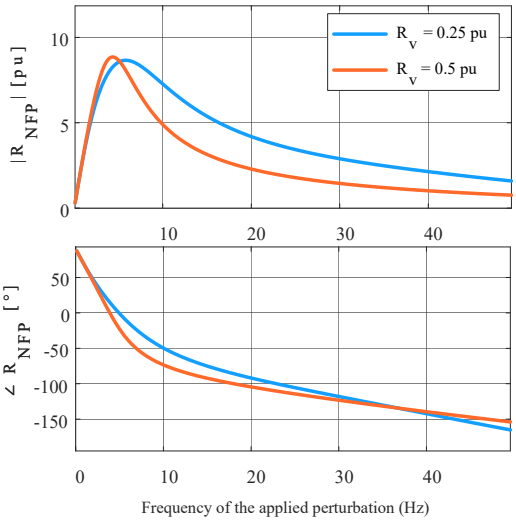
To analyze the NFP plot, it should be noted that when the phase is within the range of $+90°$ to $-90°$, power oscillation has a component which is in phase with frequency deviation, meaning a positive damping power is provided. On the other hand, when the phase of the bode plot ranges from $-90°$ to $-270°$, the damping power becomes negative. Moreover, it is worth mentioning that rapid phase changes and high magnitude in the plot are not desirable in terms of damping and should be limited [15]. Therefore, when a controller



(a)

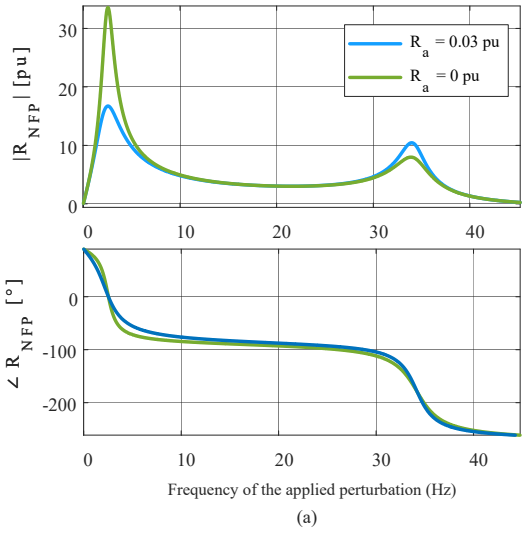


(b)

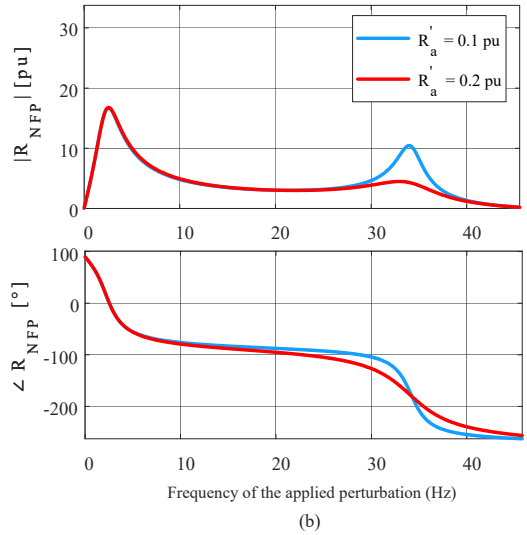


(c)

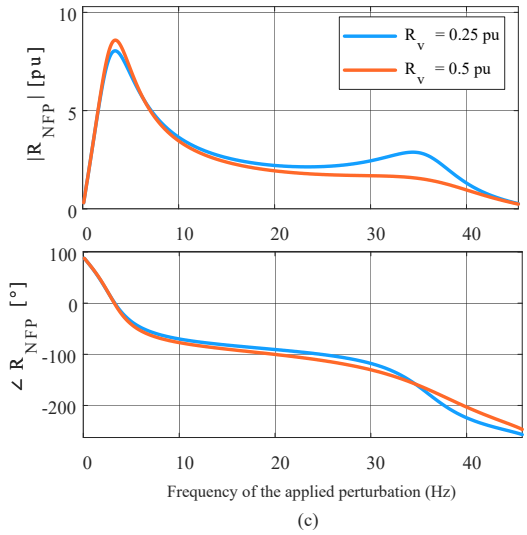
Figure 4: NFP plots of the VSC. (a) impact of active damping term (R_a) in DCCV. (b) impact of transient damping term ($R_a^{'}$) in DCCV. (c) impact of virtual resistance (R_v) in VABC.



(a)



(b)



(c)

Figure 5: NFP plots of the entire system. (a) impact of active damping term (R_a) in DCCV. (b) impact of transient damping term ($R_a^{'}$) in DCCV. (c) impact of virtual resistance (R_v) in VABC.

parameter's impact on damping is investigated, the preferred scenario occurs when the NFP plot of the converter (or the entire system) does not exhibit a high magnitude and/or an abrupt phase transition. Within the range of $+90°$ to $-90°$, this indicates more positive damping effect while within the range of $-90°$ to $-270°$, it means less negative damping effect.

The NFP plots obtained for the converter are presented in Fig. 4. It can be seen from Fig. 4(a) that active-damping term (R_a) mainly impacts low sub-synchronous frequencies, around the loop bandwidth of the active-power controller, and it enhances the damping in this region as it is implemented in the active-power controller. On the other hand, transient damping term ($R_a^{'}$) is mostly active after its high-pass filter cut-off frequency (α_{HPF}= 5Hz in this case). Therefore, it positively impacts high sub-synchronous frequencies in terms of damping, as shown in Fig. 4(b). When VABC is implemented, it can be seen from Fig. 4 (c) that the presence of the virtual resistance (R_{v}) reduces the magnitude in comparison with previous cases in the whole range, which means R_v enhances the damping. Besides, increasing R_{v} desirably lowers the magnitude and smooths the phase transition in high sub-synchronous frequencies while it can undesirably sharpen the phase shift in low sub-synchronous frequencies.

Fig. 5 illustrates the NFP plots obtained for the entire system. It can be seen that there are two resonance conditions, where the one in low sub-synchronous region is determined by the active-power controller's parameters, and is similar to mechanical mode of synchronous generator. On the other hand, the high sub-synchronous frequency is related to the electrical part of the system and is influenced by the grid and series compensator impedances. From Fig. 5(a), it can be observed that the active damping term (R_{a}) has a good impact on low sub-synchronous oscillations (around 3 Hz in this case-study), as can also be interpreted from Fig. 4(a), but it can deteriorate the dynamic of the system under study in high sub-synchronous oscillations (around 35 Hz in this case-study). On the other hand, the transient damping term ($R_{\text{a}}^{'}$) improves the damping of high sub-synchronous oscillations whereas it does not affect low sub-synchronous oscillations, as illustrated in Fig. 5(b) and interpreted from converter's NFP plot. Then, the impact of adding virtual resistance (R_{v}) in VABC strategy is shown in Fig. 5(c). It is evident that R_{v} generally enhances the damping in the whole range when compared with NFP plots of DCCV in terms of magnitude. Moreover, larger value of R_{v} increases damping in high sub-synchronous frequencies while it can have a slight undesirable impact on low sub-synchronous frequencies in this case.

B. Time-domain verification

To verify the correctness of the conducted analysis, a phase jump in the grid voltage is considered as an example case for the time-domain simulation to observe both high and low sub-synchronous oscillations.

Time-domain simulation results for different values of R_{a} in DCCV-GFM converter are illustrated in Fig 6 (a). It can be seen that with adding the active damping term, low sub-synchronous oscillation is more effectively damped while the damping of the high sub-synchronous oscillation deteriorates. This is in agreement with the corresponding NFP plots shown in Fig. 4 (a) and Fig. 5 (a).

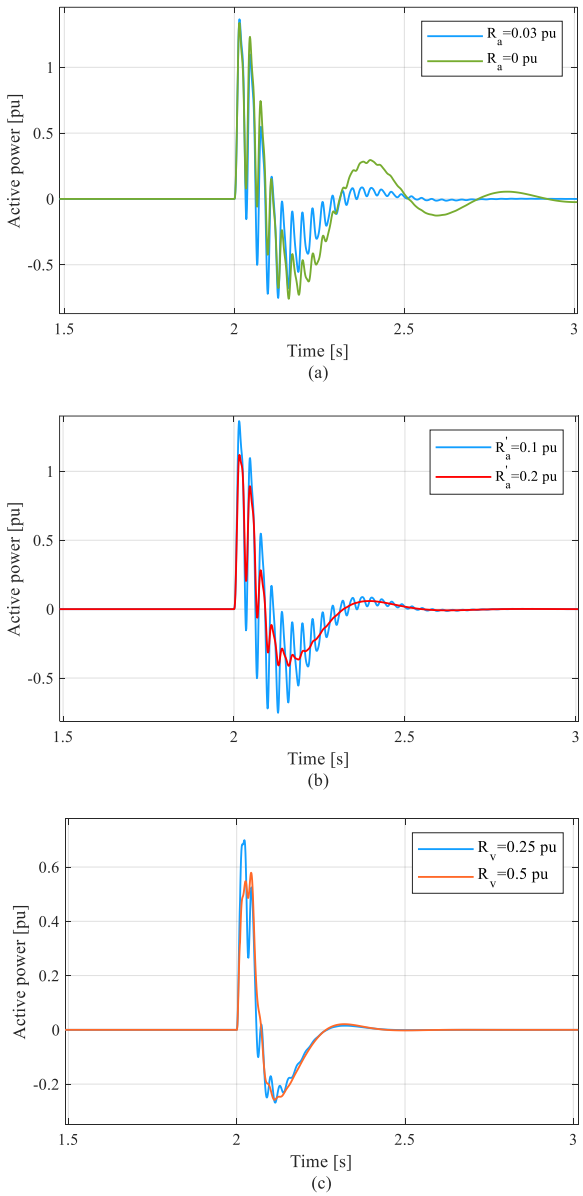


Figure 6: Time-domain simulation results. (a) impact of active damping term (R_{a}). (b) impact of transient damping term ($R_{\text{a}}^{'}$). (c) impact of virtual resistance (R_{v}).

Moreover, it can be seen from Fig. 6 (b) that increasing the transient damping term, $R_{\text{a}}^{'}$, damps the high sub-synchronous oscillation while it does not change the damping of low sub-synchronous oscillation much. Therefore, it can be concluded that this term is added to the controller to enhance the damping at high sub-synchronous frequencies. The time-domain simula-

tion result for $R_{\mathrm{a}}^{'}$, shown in Fig. 6 (b), is also in agreement with the conclusion from the corresponding NFP plots illustrated in Fig. 4 (b) and Fig. 5 (b).

Furthermore, similar to NFP plots for VABC-GFM, shown in Fig. 4 (c) and Fig. 5(c), it can be observed from Fig. 6(c) that adding virtual resistance (R_{v}) effectively damps both the high and low sub-synchronous oscillations. Moreover, when R_{v} increases, high sub-synchronous oscillations are more damped; however, increasing R_{v} can slightly deteriorate the low sub-synchronous oscillations, which is negligible in this case study.

V. Conclusion

In this paper, the impact of control parameters of two GFM control strategies, namely direct control of converter voltage (DCCV) and virtual admittance based control (VABC) on damping property of GFM converters has been investigated. Based on the analysis of the NFP plot obtained from the linearized model, it has been shown that virtual resistance and different damping terms in active-power controller and AC-voltage controller can affect high and low sub-synchronous oscillations differently. To be precise, active damping term enhances the damping in low sub-synchronous oscillations while deteriorates it in high sub-synchronous oscillations. On the other hand, transient damping term only impacts on the damping of high sub-synchronous oscillations and improves it. Moreover, virtual resistance, when VABC strategy is implemented, improves the damping in the whole range compared to DCCV. Finally, the correctness of the analysis has been validated by time-domain simulation results.

References

[1] J. Matevosyan et al., "Grid-Forming Inverters: Are They the Key for High Renewable Penetration?," in *IEEE Power and Energy Magazine*, vol. 17, no. 6, pp. 89-98, Nov.-Dec. 2019, doi: 10.1109/MPE.2019.2933072.

[2] S. Mohtat, M. Bongiorno, M. Beza and J. R. Svensson, "Impact of pole-to-pole DC voltage on energy requirement of FB YY-MMC," 2023 25th European Conference on Power Electronics and Applications, *EPE'23 ECCE Europe*, Aalborg, Denmark, 2023, pp. 1-8, doi: 10.23919/EPE23ECCEEurope58414.2023.10264684.

[3] Rocabert, J., Luna, A., Blaabjerg, F., & Rodriguez, P. (2012). "Control of power converters in AC microgrids." in *IEEE Transactions on Power Electronics*, 27(11), 4734–4749.

[4] P. Kundur, "Introduction to the Power System Stability Problem," in *Power System Stability and Control*. 1994, pp. 377–462.

[5] "Great Britain Grid Forming Best Practice Guide," National Grid ESO, Tech. Rep., 2023.

[6] S. Favuzza, R. Musca, G. Zizzo and J. A. Sa'ed, "Comparative Modeling and Analysis of EMT and Phasor RMS Grid-Forming Converters Under Different Power System Dynamics," in *IEEE Transactions on Industry Applications*, vol. 60, no. 2, pp. 3613-3624, March-April 2024, doi: 10.1109/TIA.2023.3339108.

[7] M. A. Ghadi, K. Kamalinejad, R. Razi, H. Iman-Eini and M. Hamzeh, "Stability Analysis and Enhancement of Parallel Grid-Connected Inverters with LCL Filter in A Weak Grid," *2022 12th Smart Grid Conference (SGC)*, Kerman, Iran, Islamic Republic of, 2022, pp. 1-6, doi: 10.1109/SGC58052.2022.9998891.

[8] X. Wang and F. Blaabjerg, "Harmonic Stability in Power Electronic-Based Power Systems: Concept, Modeling, and Analysis," in *IEEE Transactions on Smart Grid*, vol. 10, no. 3, pp. 2858-2870, May 2019, doi: 10.1109/TSG.2018.2812712.

[9] ENTSO-E, "High Penetration of Power Electronic Interfaced Power Sources (HPoPEIPS), ENTSO-E guidance document for national implementation for network codes on grid connection," Tech. Rep., 2017.

[10] Siemens Gamesa, "GC0137 20211122 SGRE Guide to Producing NFP plots and interpreting them R1", November 2022.

[11] "Minimum specification required for provision of GB Grid Forming (GBGF) capability (formerly Virtual Synchronous Machine/ VSM capability," National Grid ESO, Tech. Rep., 2021.

[12] A. Narula, M. Bongiorno and M. Beza, "Comparison of Grid-Forming Converter Control Strategies," *2021 IEEE Energy Conversion Congress and Exposition (ECCE)*, Vancouver, BC, Canada, 2021, pp. 361-368, doi: 10.1109/ECCE47101.2021.9594941.

[13] A. Narula, P. Imgart, M. Bongiorno, M. Beza, J. R. Svensson and J. -P. Hasler, "Voltage-Based Current Limitation Strategy to Preserve Grid-Forming Properties Under Severe Grid Disturbances," in *IEEE Open Journal of Power Electronics*, vol. 4, pp. 176-188, 2023, doi: 10.1109/OJPEL.2023.3246728.

[14] A. R. Zamani, M. H. Ghaderi and M. Hamzeh, "Dynamic Response and Filtering Capability Improvement of $\alpha\beta$-Frame Cascaded Delayed Signal Cancellation Based PLL," in *IEEE Transactions on Energy Conversion*, vol. 37, no. 2, pp. 1156-1163, June 2022, doi: 10.1109/TEC.2021.3114317.

[15] E. A. Lewis, "Enstore's updated guide for GB Grid Forming Converters-V-004", Mar. 24, 2021. Available: www.nationalgrideso.com/document/220516/download

[16] M. Yu, A. J. Roscoe, A. Dyśko, et al., "Instantaneous penetration level limits of non-synchronous devices in the British power system," *IET Renewable Power Generation*, vol. 11, no. 8, pp. 1211–1217, 2017.